An Efficient Switching Transient Analytical Model for P-GaN Gate HEMTs With Dynamic $C_G(V_{DS}, V_{GS})$

Jiahong Du, *Graduate Student Member, IEEE*, Caien Sun, *Student Member, IEEE*, Qiuyi Tang, Bomin Jiang, Zezheng Dong, *Member, IEEE*, Xinke Wu, *Senior Member, IEEE*, and Shu Yang, *Senior Member, IEEE*

***Abstract*—Accurate gate capacitance model is essentially important for switching transient analytical modeling of gallium nitride (GaN) high-electron-mobility transistor. In this article, by analyzing the charging of p-GaN/AlGaN/GaN gate structure, a dynamic gate capacitance $C_G(V_{DS}, V_{GS})$ model considering its dependence on both V_{DS} and V_{GS} is proposed, which has been validated by C_G measurement results with varying V_{DS} and V_{GS}. It has been identified in this article that the conventional static C_G model without considering its dependence on V_{GS} during switching could result in a lower C_G and underestimated Miller effect, resulting in discrepancy from the measured switching transient. By comparison, the implementation of the dynamic $C_G(V_{DS}, V_{GS})$ characteristics in the switching analytical model yields improved accuracy, by considering the two-dimensional electron gas accumulation and its impact on dynamic C_{GD} and Miller effect during switching transient. The switching transient analysis and dynamic gate capacitance $C_G(V_{DS}, V_{GS})$ characteristics are valuable for future high-frequency GaN-based power converter design.**

***Index Terms*—Capacitance-voltage, double pulse test, p-GaN gate high-electron-mobility transistors (HEMTs), switching transient modeling.**

I. Introduction

GALLIUM nitride (GaN) high-electron-mobility transistors (HEMTs) enable high-power-density and high-efficiency power converters, owing to the high switching frequency and low power losses [1], [2]. However, severe switching oscillations could occur due to the high switching speed of GaN HEMTs, resulting in overshoots of current and voltage as well as false turn-ON [3]. An accurate switching transient analytical model can provide in-depth understanding of the switching process and is essential for accurate calculation of switching transient waveforms [4], [5], [6], and thus, is particularly important for high-frequency GaN-based converter design.

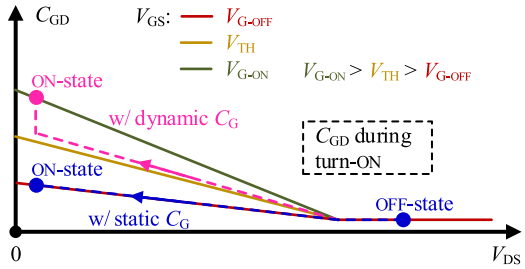

Fig. 1. Schematic C_{GD} during turn-ON transient showing the difference between considering static $C_{GD}(V_{DS})$ and dynamic $C_{GD}(V_{DS}, V_{GS})$ characteristics, respectively. $V_{G\text{-}ON}$ and $V_{G\text{-}OFF}$ are gate driver voltage supply at ON-state and OFF-state, respectively. V_{TH} is the threshold voltage of GaN HEMT.

A switching transient analytical model with junction capacitance as a function of V_{DS} [$C(V_{DS})$] has been proposed for p-GaN gate HEMTs [7], [8], [9], [10]. On the other hand, it has been found that merely implementing the static $C_{GD}(V_{DS})$ during switching transient could result in prolonged rising/falling time in SiC MOSFETs, whereas modified dynamic $C_{GD}(V_{DS})$ characteristics during switching by considering the turn-ON of gate channel could yield more accurate switching transient model [11]. It is noteworthy that static $C_{GD}(V_{DS})$ characteristics measured at a constant V_{GS} at OFF-state ($V_{G\text{-}OFF}$) are commonly used in conventional switching transient analytical modeling, whereas dynamic $C_{GD}(V_{DS}, V_{GS})$ particularly considering the influence of varying V_{GS} on C_{GD} during switching should be implemented to ensure accurate switching transient modeling (see Fig. 1).

In p-GaN gate HEMT, it is proposed that the gate capacitances C_{GS} and C_{GD} at ON-state can be obtained by multiplying a correction function by the capacitance values at OFF-state [12]. Therefore, implementing dynamic gate capacitance during switching transient would be valuable to realize accurate switching transient calculation, yet the detailed analysis of gate capacitance and quantitative $C_G(V_{DS}, V_{GS})$ modeling in p-GaN gate HEMTs are still lacking.

In this article, with detailed analysis of charge storage in the p-GaN/AlGaN/GaN gate structure, the dynamic C_G model by

Received 31 March 2024; revised 14 August 2024; accepted 11 September 2024. Date of publication 20 September 2024; date of current version 12 December 2024. This work was supported in part by the National Key Research and Development Program of China under Grant 2023YFB3611902, in part by the National Natural Science Foundation of China under Grant 52077200, in part by the Delta Power Electronics Science and Education Development Program under Grant DREK2022001, in part by the Research and Development Program of Jiangsu Province under Grant BK20232045, and in part by the Universities Collaborative Innovation Project of Anhui Province under Grant GXXT-2023-001. Recommended for publication by Associate Editor J. Hu. *(Jiahong Du, Caien Sun, and Qiuyi Tang contributed equally to this work.) (Corresponding author: Shu Yang.)*

Jiahong Du, Qiuyi Tang, Bomin Jiang, and Shu Yang are with the School of Microelectronics, University of Science and Technology of China (USTC), Hefei 230026, China (e-mail: dujiahong@mail.ustc.edu.cn; qytang@mail.ustc.edu.cn; jiangbomin@mail.ustc.edu.cn; eesyang@ustc.edu.cn).

Caien Sun, Zezheng Dong, and Xinke Wu are with the College of Electrical Engineering, Zhejiang University, Hangzhou 310013, China (e-mail: 22110078@zju.edu.cn; dongzz1218@zju.edu.cn; wuxinke@zju.edu.cn).

Color versions of one or more figures in this article are available at https://doi.org/10.1109/TPEL.2024.3465013.

Digital Object Identifier 10.1109/TPEL.2024.3465013

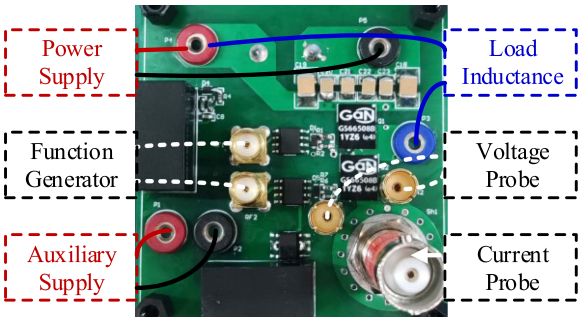

Fig. 2. DPT board for switching transient characterizations of GaN HEMTs.

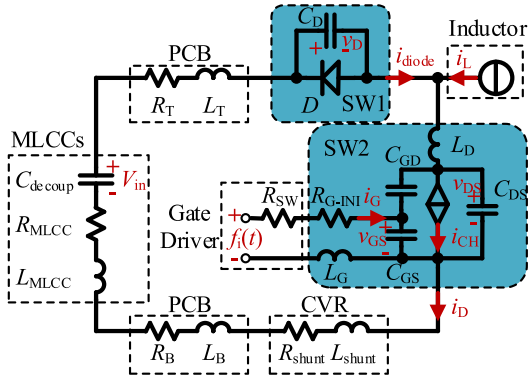

Fig. 3. Equivalent circuit of DPT circuit during switching transient. Power loop includes MLCCs, PCB, CVR, SW1, and SW2. Drive loop includes gate driver and SW2.

considering its dependence on both V_{DS} and V_{GS} ($C_G(V_{DS}, V_{GS})$) during switching transient is developed and validated by measured C_G characteristics with varying V_{DS} and V_{GS}. The calculated switching transients by implementing the proposed dynamic $C_G(V_{GS}, V_{DS})$ model and the conventional static $C_G(V_{DS})$ model as in the state-of-the-art prior works have been compared and analyzed. The proposed dynamic C_G model is implemented in switching transient analytical model, which yields improved accuracy compared with the conventional static C_G model. The impact of the two-dimensional electron gas (2DEG) accumulation and its impact on dynamic C_G and Miller effect during switching transient are also analyzed and revealed.

II. Switching Transient Modeling

The switching transient of GaN HEMTs are characterized using a custom-designed double pulse tester (DPT) [13] (see Fig. 2). Fig. 3 shows the equivalent circuit of the DPT during switching transient, in which the main components are modeled as follows.

1) The GaN HEMT is modeled according to its measured current-voltage and capacitance-voltage characteristics, which will be discussed in detail in Section III.

2) The current viewing resistor (CVR) SSDN-10 is modeled by a resistor and inductor in series [14].

3) The load inductor is modeled by a constant current source with its parasitic capacitance considered into C_D.

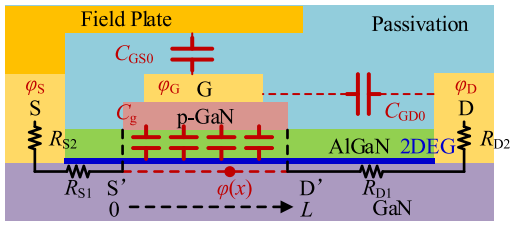

Fig. 4. Schematic of a p-GaN gate HEMT, where C_g is the capacitance between gate and 2DEG channel per unit area, L is gate length, R_{S1} and R_{D1} are access region resistances, and R_{S2} and R_{D2} are contact resistances.

4) The gate driver is modeled by a switching resistor R_{SW} to which a step voltage is applied.

5) The multilayer ceramic chip capacitors (MLCCs), acting as decoupling capacitors, are modeled by capacitance, resistance and inductance in series. The parasitic parameters of the printed circuit board (PCB) are derived by Ansys simulations.

Based on Kirchhoff's current law (KCL) and Kirchhoff's voltage law (KVL), the equivalent circuit can be described by

$$\begin{cases} V_G = v_{GS} + L_G \frac{di_G}{dt} + R_G i_G \\ V_{in} = v_{DS} + v_D + L_{loop} \cdot \frac{di_D}{dt} + R_{loop} \cdot i_D - R_T \cdot i_L \\ i_D = C_D \frac{dv_D}{dt} + i_{diode} + i_L \\ i_D = C_{DS} \frac{dv_{DS}}{dt} - C_{GD} \frac{dv_{GD}}{dt} + i_{CH} \\ i_G = C_{GS} \frac{dv_{GS}}{dt} + C_{GD} \frac{dv_{GD}}{dt} \end{cases} \quad (1)$$

where L_{loop} is the sum of the package inductance of GaN HEMT at drain (L_D), parasitic inductance of current shunt (L_{shunt}), MLCCs (L_{MLCC}) and PCB (L_B and L_T). Additionally, R_{loop} is the sum of the parasitic resistances of MLCCs (R_{MLCC}) as well as PCB (R_B and R_T). R_G is the sum of the switching resistance (R_{SW}) and internal gate resistance ($R_{G\text{-}INI}$) of GaN HEMT. Accordingly, state equations at turn-ON/OFF transient and their time-domain solutions can be determined by iterative methods, which can be used for switching transient modeling [7].

The voltage waveforms of GaN HEMT are captured by a voltage probe connecting to an oscilloscope channel with a bandwidth of 500 MHz. The current waveforms of GaN HEMT are captured by CVR with a bandwidth of 1.6 GHz connecting to an oscilloscope channel with a bandwidth of 1 GHz, which yields an equivalent bandwidth of ~850 MHz for current measurements.

III. GaN HEMT Modeling With Dynamic Gate Capacitance

A. Current-Voltage Characteristics

Device under test in this article is a 650 V commercial p-GaN gate HEMT with threshold voltage (V_{TH}) of ~1.7 V. Schematic of the p-GaN gate HEMT is shown in Fig. 4, in which S′ and D′ represent the source-side and drain-side gate edges, respectively. Current-voltage characteristics of GaN HEMT are modeled based on piecewise linear model [15], in which the channel current $I_D(V_{DS}, V_{GS})$ characteristics in linear and saturation regions are represented by a V_{GS}-dependent resistor and

V_{GS}-controlled current source, respectively, which are described by

$$\begin{cases} I_D = \mu C_g \frac{W}{L} V_{GT} [V_{DS} - (R_S + R_D) I_D] \\ I_{D-SAT} = \mu C_g \frac{W}{L} V_{TH} \left[\sqrt{V_{TH}^2 + (V_{GT} - R_S I_{D-SAT})} - V_L \right] \end{cases} \quad (2)$$

where μ is electron mobility in 2DEG, W is gate width, $V_{GT} = V_{GS'} - V_{TH}$, $R_S = R_{S1} + R_{S2}$, $R_D = R_{D1} + R_{D2}$, $V_L = F_S \cdot L$, and F_S is saturation electric field.

Based on (2), a behavior model of current-voltage characteristics can be expressed by

$$\begin{cases} I_{DS} = S_{ON}(V_{GS}) \cdot V_{DS} \\ I_{D-SDT} = I_{D-SAT}(V_{GS}) \end{cases} \quad (3)$$

where $S_{ON}(V_{GS})$ represents the conductance of GaN HEMT in linear region, and $I_{D\text{-}SAT}(V_{GS})$ represents the current in saturation region. $S_{ON}(V_{GS})$ and $I_{D\text{-}SAT}(V_{GS})$ could be extracted from output and transfer characteristics.

B. Dynamic Gate Capacitance Model

Modeling the influence of V_{DS} and V_{GS} on C_{GS} and C_{GD} during switching transient (i.e., dynamic gate capacitance) is particularly important for accurate switching transient analysis. However, it is challenging to distinguish and separately extract C_{GD} and C_{GS} when the 2DEG channel is formed. On the other hand, Meyer capacitance model, considering the impact of V_{DS} on the non-uniform charge distribution along the channel and gate capacitance, has been implemented to distinguish C_{GS} and C_{GD} in Si MOSFET for logic applications [16].

In the p-GaN gate HEMT (see Fig. 4), the potential at a certain point x along 2DEG channel is $\varphi(x)$. The electron density n_{2DEG} at x could be described by

$$n_{2DEG} = C_g(\varphi_G - \varphi(x) - V_{TH}). \quad (4)$$

Gate-to-channel charge Q_G is given by

$$Q_G = W \int_0^L n_{2DEG} \, dx. \quad (5)$$

Based on linear velocity-field relation, the drain current I_D is

$$I_D = \mu W n_{2DEG} \frac{d\varphi(x)}{dx}. \quad (6)$$

From (4) and (6), I_D could be expressed as

$$I_D = \mu C_g \frac{W}{L} \left(V_{GT} V_{D'S'} - \frac{1}{2} V_{D'S'}^2 \right) \quad (7)$$

Based on (5), Q_G can be represented by integration of $\varphi(x)$

$$\begin{aligned} Q_G &= W \int_0^{V_{D'S'}} n_{2DEG} \frac{dx}{d\varphi(x)} d\varphi(x) \\ &= C_G \frac{V_{GT}^2 - V_{GT} V_{D'S'} + V_{D'S'}^2/3}{V_{GT} - V_{D'S'}/2} \end{aligned} \quad (8)$$

where n_{2DEG} can be derived from (4), $dx/d\varphi(x)$ can be obtained from (6) and (7), C_G is equal to $C_g WL$

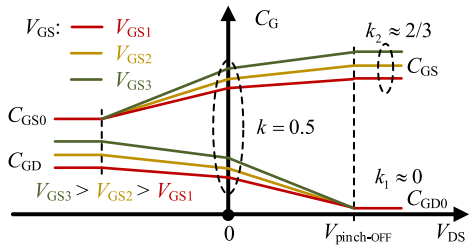

Fig. 5. Schematic C_G-V_{DS} characteristic for p-GaN gate HEMT, where $V_{pinch\text{-}OFF}$ is the value of V_{DS} when the drain-side gate edge is pinched-OFF (i.e., $V_{D'S'}$ equals to V_{GT}).

Accordingly, C_{GD} and C_{GS} could be expressed as

$$\begin{aligned} C_{GD} &= \frac{\partial Q_G}{\partial V_{GD'}} \cdot \frac{\partial V_{GD'}}{\partial V_{GD}} \\ &= \frac{2}{3} C_G \left(1 - \frac{V_{GT}^2}{(2V_{GT} - V_{D'S'})^2} \right) \cdot \left(1 + R_D \frac{\partial I_D}{\partial V_{GD}} \right) \end{aligned} \quad (9)$$

$$\begin{aligned} C_{GS} &= \frac{\partial Q_G}{\partial V_{GS'}} \cdot \frac{\partial V_{GS'}}{\partial V_{GS}} \\ &= \frac{2}{3} C_G \left(1 - \frac{(V_{GT} - V_{D'S'})^2}{(2V_{GT} - V_{D'S'})^2} \right) \cdot \left(1 - R_S \frac{\partial I_D}{\partial V_{GS}} \right). \end{aligned} \quad (10)$$

$\partial Q_G/\partial V_{GD'}$ and $\partial V_{GD'}/\partial V_{GD}$ are denoted by part A and part B as follows:

$$\begin{cases} \text{PartA} = \frac{\partial Q_G}{\partial V_{GD'}} = \frac{2}{3} C_G \left(1 - \frac{V_{GT}^2}{(2V_{GT} - V_{D'S'})^2} \right) \\ \text{PartB} = \frac{\partial V_{GD'}}{\partial V_{GD}} = \left(1 + R_D \frac{\partial I_D}{\partial V_{GD}} \right) \end{cases}. \quad (11)$$

$\partial Q_G/\partial V_{GS'}$ and $\partial V_{GS'}/\partial V_{GS}$ are denoted by part C and part D as follows:

$$\begin{cases} \text{PartC} = \frac{\partial Q_G}{\partial V_{GS'}} = \frac{2}{3} C_G \left(1 - \frac{(V_{GT} - V_{D'S'})^2}{(2V_{GT} - V_{D'S'})^2} \right) \\ \text{PartD} = \frac{\partial V_{GS'}}{\partial V_{GS}} = \left(1 - R_S \frac{\partial I_D}{\partial V_{GS}} \right) \end{cases}. \quad (12)$$

Note that in linear region ($V_{D'S'} \leq V_{GT}$), C_{GD} and C_{GS} could be expressed as (9) and (10). In saturation region ($V_{D'S'} \geq V_{GT}$), part A and part C maintain constant.

According to (9) and (10), the schematic C_G-V_{DS} curves as shown in Fig. 5 are analyzed and discussed as follows.

1) At V_{DS} of 0 V, part A and part C are equal to $1/2 \cdot C_G$, whereas part B and part D are equal to 1, according to (9) and (10). In this case, $k(V_{DS})$ is 0.5.
2) As $V_{D'S'}$ is approaching V_{GT}, part A is approaching zero, according to (9). At relatively high V_{DS} at OFF-state or during switching, the majority of high V_{DS} could drop across the gate-to-drain access region in high-voltage p-GaN gate HEMT, yielding a smaller $V_{D'S'}$ than V_{DS}. In a special case, when $V_{D'S'}$ is equal to V_{GT}, D′ is pinched-OFF and n_{2DEG} at D′ is zero, as shown in Fig. 6. In this case, this specific value of V_{DS} is denoted as $V_{pinch\text{-}OFF}$ in Fig. 5. In practice, field plates that are commonly

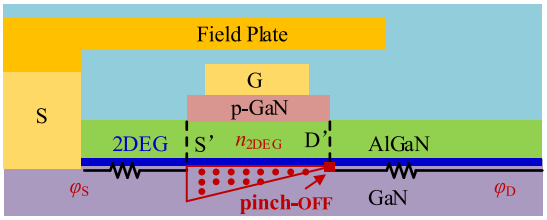

Fig. 6. Schematic of p-GaN gate HEMT in saturation region showing that D′ is pinched-OFF.

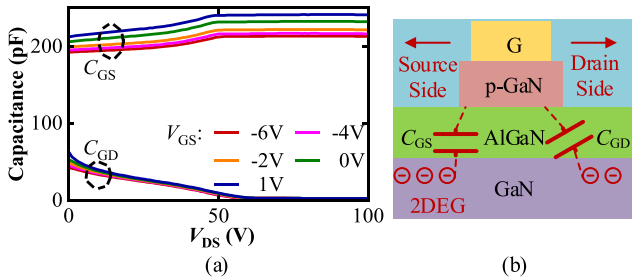

Fig. 7. (a) Measured C_G-V_{DS} characteristics with varying V_{GS}. (b) Illustration of the depletion region capacitances at source-side and drain-side at OFF-state with $V_{DS} > 0$ V.

used in GaN HEMTs [17] can spread out potential along the gate-to-drain access region (see Fig. 6). For part B, when p-GaN gate HEMT is operating in saturation region with a relatively large V_{DS}, $\partial I_D/\partial V_{GD}$ equals to zero. Consequently, when V_{DS} reaches $V_{\text{pinch-OFF}}$, $k_1(V_{DS})$ is approximately equal to zero in Fig. 5.

3) In (10), as $V_{D'S'}$ reaches V_{GT}, part C increases to 2/3·C_G. In part D, R_S includes contact resistance at source terminal and gate-to-source access region resistance. R_S is estimated to constitute ∼5% of the total R_{ON} [18], [19]. Moreover, according to the electrical characteristics of the GaN HEMT used in this work [20], R_{ON} multiplied by $\partial i_D/\partial V_{GS}$ (i.e., Part D) is varying from 0.9 to 1.0. As a result, $k_2(V_{DS})$ is approximately 2/3 at V_{DS} of $V_{\text{pinch-OFF}}$, as shown in Fig. 5.

The dependence of C_{GS} and C_{GD} on V_{DS} can be expressed by $k(V_{DS})$·C_G behavior model. In addition to the dependence of C_{GS} and C_{GD} on V_{DS}, C_G in (9) and (10), which is the capacitance of metal/p-GaN/AlGaN/GaN gate structure, also varies with gate bias V_G. This relationship between C_G and gate voltage bias is extracted as $C_G(V_{GS})$, which is responsible for the dispersion among C_G-V_{DS} curves with various V_{GS} as in Fig. 5.

Considering the dependence of C_G on V_{DS} ($k(V_{DS})$) as well as the dependence of C_G on gate bias ($C_G(V_{GS})$), the proposed dynamic capacitance model is given by

$$\begin{bmatrix} C_{GD}(V_{DS}, V_{GS}) \\ C_{GS}(V_{DS}, V_{GS}) \end{bmatrix} = \begin{bmatrix} C_{GD0} \\ C_{GS0} \end{bmatrix} + \begin{bmatrix} k_1(V_{DS}) \cdot C_G(V_{GS}) \\ k_2(V_{DS}) \cdot C_G(V_{GS}) \end{bmatrix} \quad (13)$$

where C_{GD0} and C_{GS0} are capacitances between electrode metals, as shown in Fig. 4.

C. Validation of the Dynamic Capacitance Model

Fig. 7(a) shows the measured C_{GS}-V_{DS} and C_{GD}-V_{DS} characteristics of p-GaN gate HEMT, which are in qualitative agreement with the trend of the theoretical C_{GS}-V_{DS} and C_{GD}-V_{DS} behaviors as in Fig. 5. Consistent with the nonuniform charging of Q_G at nonzero V_{DS}, the dependence of C_{GS} and C_{GD} on V_{DS} could also be illustrated by the evolvement of the depletion region at the gate edges, as shown in Fig. 7(b). With increased V_{DS}, edge capacitance at drain side C_{GD} decreases as depletion region extends toward drain side, whereas C_{GS} rises. Such dependence of C_G on V_{DS} is modeled by $k(V_{DS})$ as in (13). Moreover, there is V_{GS}–induced dispersion among C_G-V_{DS} curves, as the increased V_{GS} leads to accumulated 2DEG and increased C_G.

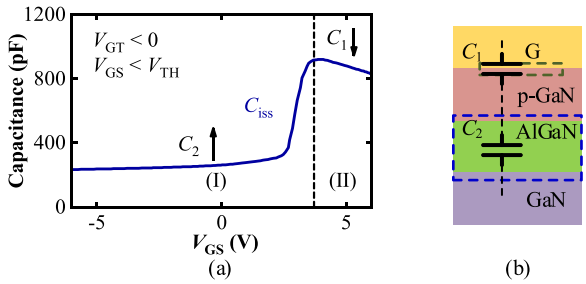

Fig. 8. (a) Measured C_{iss}-V_{GS} characteristics at $V_{DS} = 0$ V. (b) Schematic of Schottky metal/p-GaN/AlGaN/GaN gate structure in p-GaN gate HEMT.

In the measured C_{iss}-V_{GS} characteristics [see Fig. 8(a)], there is a rising slope corresponding to the formation of 2DEG channel, whereas C_{iss} decreases with further increased V_{GS}. As shown in Fig. 8(b), C_{iss} of the metal/p-GaN/AlGaN/GaN gate stack consists of the capacitances corresponding to metal/p-GaN Schottky junction (C_1) and p-GaN/AlGaN/GaN heterojunction (C_2) in series. When V_{GS} is relatively low (i.e., $< V_{TH}$), the increasing V_{GS} induces accumulated electrons in the 2DEG channel, and increased C_2. After the turn-ON of 2DEG channel, further increased V_{GS} leads to depletion region extension in the reversely biased Schottky junction at metal/p-GaN, and consequently decreased C_1. The dependence of C_{iss} on V_{GS} is modeled by $C_G(V_{GS})$ in (13).

The calculated C_G-V_{DS} curves using the abovementioned dynamic C_G model agree well with the measurement results, as shown in Fig. 9. In particular, the calculated C_G-V_{DS} curves featuring dynamic C_G model during switching transient exhibit distinction from that calculated with the conventional static C_G model (i.e., without considering the dependence of C_G on V_{GS}), as shown in Fig. 10. It suggests that it is essentially important to consider and implement dynamic C_G model for accurate switching transient modeling.

IV. Implementation of the Analytical Model

Based on the equivalent circuit as shown in Fig. 3, state equations are determined, and iterative method is employed to derive the time-domain switching waveforms. Furthermore,

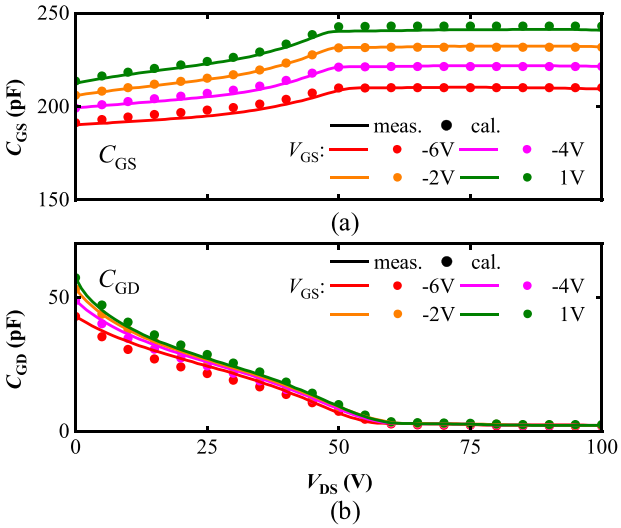

Fig. 9. Measured and calculated (a) C_{GS}-V_{DS} and (b) C_{GD}-V_{DS} curves with varying V_{GS}.

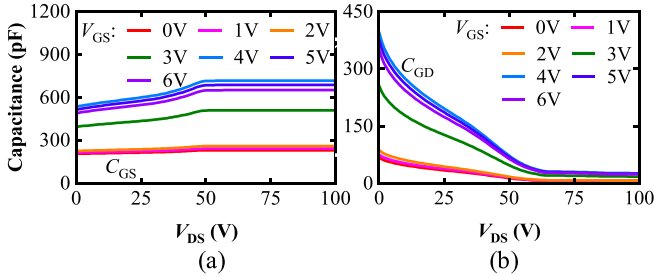

Fig. 10. (a) C_{GS} and (b) C_{GD} calculated by the proposed dynamic C_G model across a range of V_{GS} at OFF-state as well as ON-state. C_G-V_{DS} curve at V_{GS} of 0 V corresponds to the conventional static $C_G(V_{DS})$ characteristics.

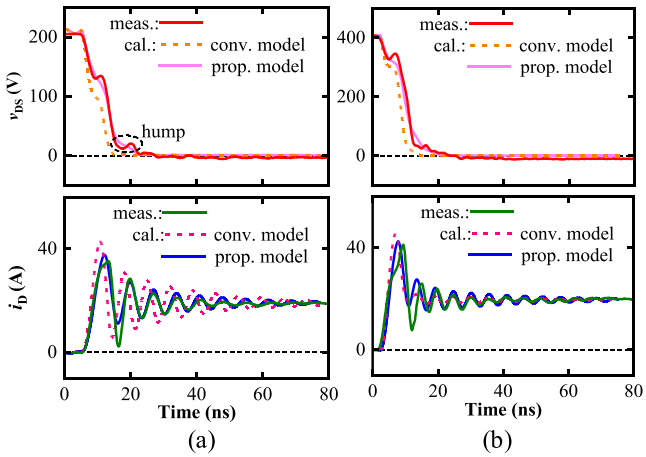

Fig. 11. Measured and calculated switching transient waveforms of turn-ON transient with varying V_{DS} of (a) 200 V and (b) 400 V, respectively.

TABLE I
COMPARISON OF WAVEFORMS DURING TURN-ON CALCULATED WITH STATIC AND DYNAMIC C_G CHARACTERISTICS

	Voltage	Measured	W/ static C_G	W/ dynamic C_G
t_F of v_{DS} at turn-ON	200 V	15.6 ns	8.0 ns (-49%)	14.4 ns (-8%)
	400 V	17.7 ns	10.4 ns (-41%)	16.2 ns (-8%)
t_R of i_D at turn-ON	200 V	3.2 ns	2.4 ns (-25%)	3.4 ns (+6%)
	400 V	2.9 ns	1.8 ns (-61%)	2.5 ns (-22%)
i_{D_PK} at turn-ON	200 V	35 A	43 A (23%)	38 A (+9%)
	400 V	41 A	44 A (7%)	40 A (-2%)
Freq. of resonance	200 V	142 MHz	144 MHz	142 MHz
	400 V	196 MHz	185 MHz	181 MHz

Remarks: (±X%) is the error ratio, which is the difference between the measured and calculated values, i.e., (Cal.-Meas.)/Meas.

conventional static C_G model and the proposed dynamic C_G model are implemented in the switching transient analysis, respectively.

With conventional static C_G model extracted at V_{GS} of 0 V, the calculated v_{DS} decreases more significantly than the measured switching waveform, as shown in Fig. 11. Moreover, peak value of the calculated i_D (i_{D_PK}) is higher than the measured waveform. With dynamic C_G implemented by considering increased C_{GD} at ON-state, the calculated v_{DS} waveform shows better agreement with the measured turn-ON waveform. Compared with the calculated waveforms using the conventional static C_G model, implementing the proposed dynamic C_G model in this article can suppress the error ratio (i.e., difference between the measured and calculated values divided by the measured value) of falling-time (during which, the value decreases from 90% to 10%) (t_F) of v_{DS} during turn-ON by ~30%, and that of i_{D_PK} during turn-ON by ~10%, as given in Table I. When v_{GS} approaches V_{TH} and v_{DS} starts decreasing, clear difference of C_{GD} between static and dynamic C_G model is shown in Fig. 10(b), which could illustrate those improvements on switching transient calculated at turn-ON. C_G of GaN HEMT is lower when switching from higher V_{DS}, resulting in higher frequency of resonance at higher V_{DS} of 400 V. In practice, the accuracy of the measured frequency of resonance is slightly reduced at V_{DS} of 400 V. It is practically inevitable that the measurement range of the probe would slightly reduce at higher frequency. On the other hand, when switching under higher V_{DS} condition, the waveforms usually have wider voltage/current range, while the resolution of the measured voltage/current could be limited by the oscilloscope [21].

In particular, Fig. 12 shows the switching transient waveforms calculated with static C_G and dynamic C_G models at switching from V_{DS} of 200 V, respectively. The turn-ON process herein can be divided into four stages.

1) Stage I corresponds to the charging process of C_{iss} with high v_{DS} and low v_{GS}. In this case, implementing dynamic C_G and static C_G models yield insignificant distinctions in the waveforms, as shown in Fig. 12.
2) In stage II, compared with the measured waveforms, v_{DS} waveforms calculated with static C_G model decrease faster and i_D waveforms rise faster. Miller effect takes place in this stage with v_{GS} clamped at a value that is slightly higher than V_{TH}. With the proposed dynamic C_G model, the higher calculated C_{GD} can result in wider Miller plateau

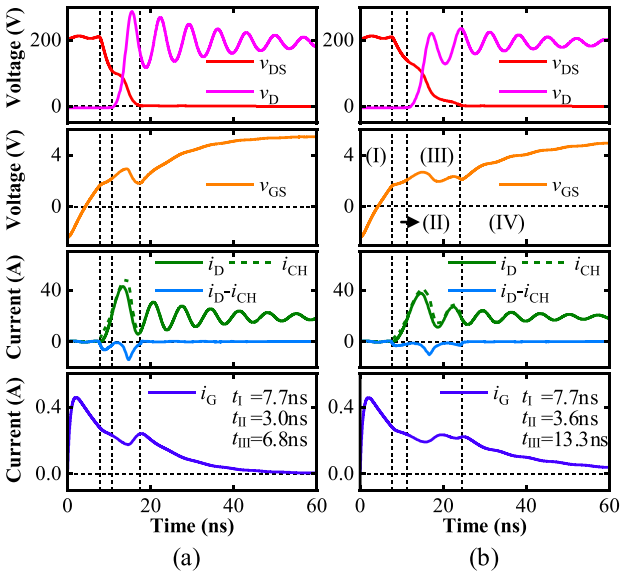

Fig. 12. Detailed analysis of switching transient at turn-ON calculated with (a) static and (b) dynamic C_G characteristics. t_I, t_{II}, and t_{III} are durations of stages I, II, and III, respectively.

[see Fig. 10(b)], reduced dv_{DS}/dt and di_D/dt, yielding better agreement with the measured waveforms.

3) In stage III, Miller effect still exists, while v_{GS} and i_{CH} can reach their peak values. Because of the evident distinction between static C_G and dynamic C_G curves particularly at V_{GS} larger than V_{TH} (e.g., $>$ 2 V) as shown in Fig. 10, the switching waveforms calculated with the static and dynamic C_G models exhibit significant distinction, as shown in Fig. 12. In particular, with the dynamic model, i_{D_PK} is reduced and t_{III} (time of duration in stage III) is increased as a result of the extended Miller plateau with higher calculated C_{GD}, yielding a better agreement with the measured turn-ON waveforms [see Fig. 11(a)]. Moreover, unlike that of static C_G model, there is a hump in v_{DS} waveform [see Fig. 11(a)] calculated with dynamic C_G model in stage III with prolonged t_{III}, which is consistent with the measured switching waveforms [see Fig. 11(a)].
4) In stage IV, C_{iss} is charged at low v_{DS} and high v_{GS}. Similar with that in stage I, implementing dynamic C_G model yields lower dv_{GS}/dt, compared with that using static model, as shown in Fig. 12(b).

In addition to the measurements and modeling with I_D of 20 A, switching transient measurements and modeling with I_D of 10 and 15 A have also been carried out, respectively. Compared with the conventional static C_G model, the proposed dynamic C_G model can yield lower i_{D_PK} and better agreement with the measured switching waveforms with switching current of 10 and 15 A (see Fig. 13). When v_{GS} is clamped at Miller plateau voltage during switching transients, the higher C_{GD} calculated with the proposed dynamic C_G model can lead to wider Miller plateau, lower dv_{DS}/dt and di_D/dt, leading to better agreement with the measured switching waveforms.

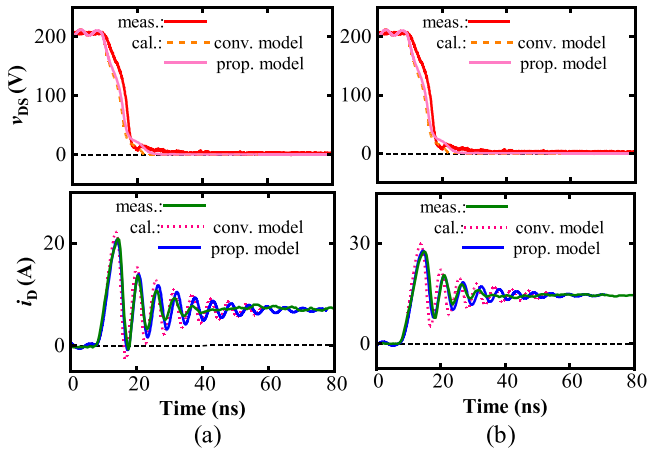

Fig. 13. Measured and calculated switching transient waveforms of turn-ON transient with varying I_D of (a) 10 A and (b) 15 A, respectively.

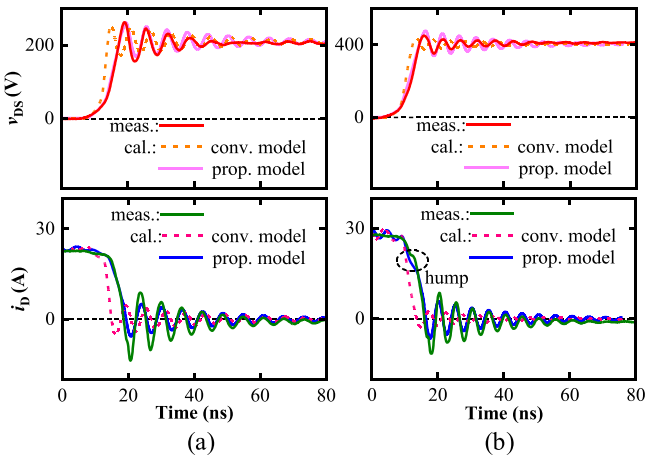

Fig. 14. Measured and calculated switching transient waveforms of turn-OFF transient with varying V_{DS} of (a) 200 V and (b) 400 V, respectively.

The GaN HEMT undergoes low v_{DS} and high v_{GS} before turning-OFF. In this case, the distinction between dynamic C_G and static C_G is significant, as shown in Fig. 10. And thus, the dependence of C_G on V_{GS} (or the dynamic C_G model) should be considered. Compared with the conventional static C_G model extracted at V_{GS} of 0 V, implementing the dynamic C_G model can yield better agreement with the measured switching waveforms at turn-OFF, as shown in Fig. 14. However, the increase of C_{GD} in Fig. 10 leads to a distinction between the switching waveforms calculated with static C_G and dynamic C_G. As shown in Table II, implementing the proposed dynamic C_G model can deliver ~30% improvement in the accuracy of the rising-time (during which, the value increases from 10% to 90%) (t_R) of v_{DS}, and ~10% improvement in that of the peak value of i_D (i_{D_PK}).

Fig. 15 shows the switching transient waveforms calculated with static C_G and dynamic C_G models during turn-OFF transient with V_{DS} of 400 V. Similar with the turn-ON process, the turn-OFF process can be primarily divided into four stages.

1) Stage I corresponds to the discharging process of C_{iss} with low v_{DS} and high v_{GS}. In this case, implementing

TABLE II
COMPARISON OF WAVEFORMS DURING TURN-OFF CALCULATED WITH STATIC AND DYNAMIC C_G MODEL

	Voltage	Measured	W/ static C_G	W/ dynamic C_G
t_R of v_{DS} at turn-OFF	200 V	6.3 ns	3.7 ns (-41%)	6.4 ns (+2%)
	400 V	7.9 ns	5.7 ns (-28%)	8.3 ns (+5%)
t_F of i_D at turn-OFF	200 V	5 ns	4.2 ns (-16%)	5.4 ns (+8%)
	400 V	5.4 ns	3.4 ns (-37%)	6.1 ns (+13%)
v_{DS_PK} at turn-OFF	200 V	263 V	255 V (-3%)	262 V (0%)
	400 V	450 V	434 V (-4%)	476 V (+6%)
i_{D_PK} at turn-OFF	200 V	8.8 A	4.5 A (-49%)	5 A (-43%)
	400 V	8.6 A	2.4 A (-72%)	5.7 A (-34%)
Freq. of resonance	200 V	159 MHz	158 MHz	160 MHz
	400 V	196 MHz	195 MHz	193 MHz

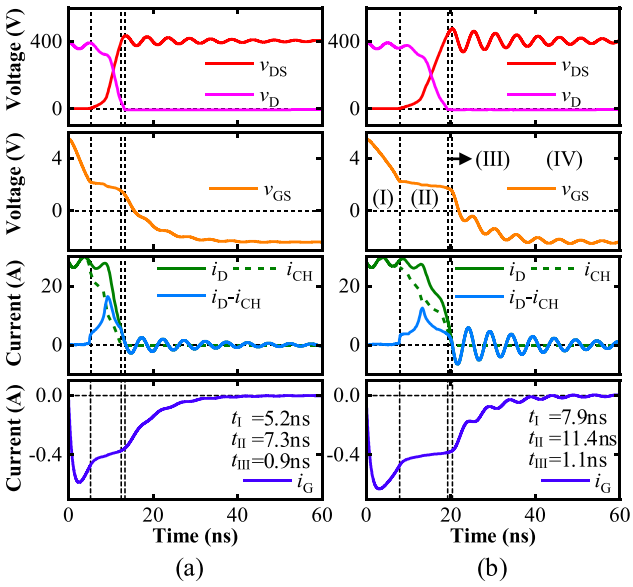

Fig. 15. Detailed analysis of switching transient at turn-OFF calculated with (a) static and (b) dynamic C_G characteristics. t_I, t_{II}, and t_{III} are durations of stages I, II, and III, respectively.

dynamic C_G and static C_G models can yield significant distinctions in the waveforms (see Fig. 15). In particular, with the dynamic model, the time of duration in stage I (t_I) is increased as a result of the larger C_{iss}, as shown in Fig. 15. Consequently, the calculated v_{GS} waveforms with the dynamic C_G model can deliver reduced dv_{GS}/dt during C_{iss} discharging, which is more consistent with the measured waveforms.

2) In stage II, power loop and drive loop in Fig. 3 are coupled and v_{GS} is clamped. Additionally, there is resonance between C_D, C_{DS}, and L_{loop}. In the calculated switching waveforms with dynamic C_G characteristics, there is a hump in i_D waveforms [see Fig. 14(b)], which is consistent with the measured switching waveforms. However, such feature as in the measured waveforms is absent in the calculated switching transient with conventional static C_G.

3) Stage III can be generally categorized into two cases [7]: i) If i_{CH} drops to 0 A, while v_D has not yet decreased to the reverse conduction voltage drop of SW1 in Fig. 3, the power loop would decouple with the drive loop initially. This case corresponds to the waveforms calculated with static C_G characteristics [see Fig. 15(a)]. ii) Alternatively, when C_{DS} decouples with L_{loop} initially, it corresponds to the waveforms calculated with dynamic C_G characteristics [see Fig. 15(b)]. It is found that the waveforms in case ii) agree well with the measured waveforms, as shown in Fig. 14(b). In other words, switching waveforms calculated with conventional static C_G model could result in error in the turn-OFF transient.

4) In stage IV, C_{iss} is discharged at high v_{DS} and low v_{GS}. In this case, implementing dynamic C_G and static C_G models yield insignificant distinctions in the waveforms, as shown in Fig. 15.

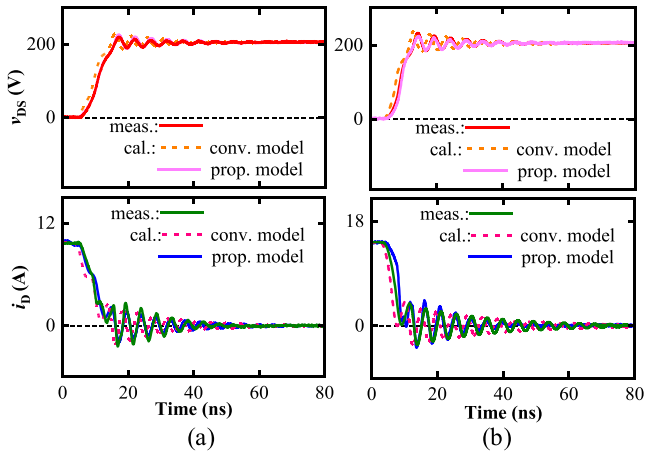

Fig. 16. Measured and calculated switching transient waveforms of turn-OFF transient with varying I_D of (a) 10 A and (b) 15 A, respectively.

As shown in Fig. 16, the deviation of the calculated waveforms with the conventional static C_G model from the measured waveforms is possibly attributed to the underestimated C_G in the conventional static C_G model during switching transient. By implementing the proposed dynamic C_G model, the dependence of dynamic C_G on V_{GS} and V_{DS} has been taken into consideration. And thus, the discharging process of larger C_{iss} with low v_{DS} and high v_{GS} can lead to lower dv_{DS}/dt and i_{D_PK} with the proposed dynamic C_G model. Therefore, the proposed model with dynamic C_G can yield better agreement with the measured switching waveforms during turn-ON/OFF transient with varying switching current.

The gate charge (Q_G) is a critical parameter that could influence the switching transients, which primarily includes gate-to-source charge (Q_{GS}) and gate-to-drain charge (Q_{GD}). In particular, the switching transients are associated with charging and discharging of the C_{GD}. When C_{GS} is charged until Miller plateau is reached, V_{GS} can be clamped at a value slightly higher than V_{TH} with C_{GS} completely charged, and C_{GD} is charged by

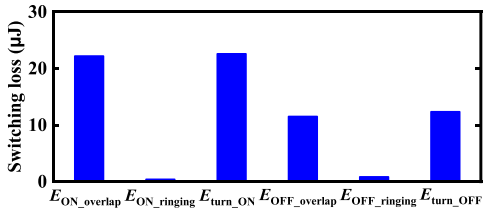

Fig. 17. Measured switching loss components with V_{DS} of 200 V and I_D of 20 A. Turn-ON switching loss (E_{turn_ON}) and turn-OFF switching loss (E_{turn_OFF}) primarily include OFF-to-ON overlap loss ($E_{ON\_overlap}$), OFF-to-ON ringing loss ($E_{ON\_ringing}$), ON-to-OFF overlap loss ($E_{OFF\_overlap}$), ON-to-OFF ringing loss ($E_{OFF\_ringing}$), respectively.

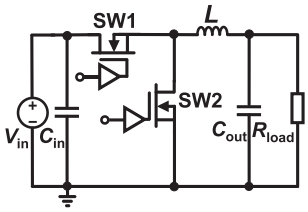

Fig. 18. Schematic diagram of the DC–DC buck converter.

i_G. Different from the conventional model with static C_G, the proposed dynamic C_G model exhibits wider Miller plateau in stages II and III (see Fig. 12) by considering the influence of V_{GS} on C_G, yielding a better agreement with the measured turn-ON waveforms in Fig. 11(a). The calculated Q_G values at turn-ON transient with conventional static C_G model and the proposed dynamic C_G model are 7.35 and 7.80 nC, respectively. Similarly, the calculated Q_G values at turn-OFF transient [see Fig. 14(a)] with conventional static C_G model and the proposed dynamic C_G model are 5.12 and 5.16 nC, respectively. In summary, unlike the conventional static C_G model in which Q_G could be underestimated, the proposed dynamic C_G model can yield larger Q_G by considering the influence of V_{GS} on C_G during switching transients.

As shown in Fig. 17, from the measured switching transients with V_{DS} of 200 V and I_D of 20 A, the turn-ON switching loss (E_{turn_ON}) and turn-OFF switching loss (E_{turn_OFF}) are extracted to be 22.5 and 12.3 μJ, respectively. Compared with the conventional static C_G model yielding E_{turn_ON} of 16.8 μJ and E_{turn_OFF} of 7.5 μJ, implementing the proposed dynamic C_G model in this article can deliver E_{turn_ON} of 17.2 μJ and E_{turn_OFF} of 13.9 μJ, suppressing the error ratio by $\sim$26% for E_{turn_OFF} and by $\sim$2% for E_{turn_ON}, respectively.

As shown in Fig. 18, the proposed dynamic C_G model is implemented and validated in a dc–dc buck converter. The converter operates at an input voltage of 180 V, an output voltage of 80 V, and an output current of 7 A with a switching frequency of 1 MHz. As shown in Fig. 18, the capacitor (C_{in}) is precharged by the dc power supply voltage (V_{in}) before turning ON the high-side GaN HEMT (SW1). After the SW1 is turned ON with the low-side GaN HEMT (SW2) at OFF-state, load inductance (L) is charged by V_{in} and current flowing through the L increases linearly. Then the SW1 is turned OFF and SW2 is turned ON to operate in reverse conduction mode. When SW1 is turned

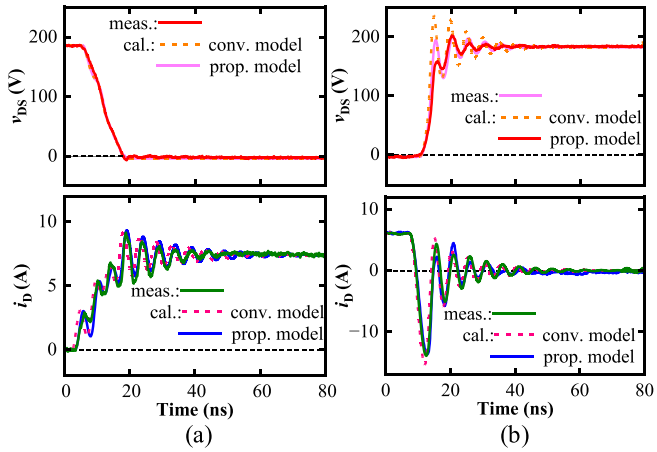

Fig. 19. Measured and calculated switching transient waveforms of the low-side GaN HEMT (SW2) operates in DC–DC buck converter at (a) turn-ON and (b) turn-OFF.

ON again with SW2 at OFF-state, the current continues to flow through SW1.

The switching transient behaviors of SW2 have been measured and calculated by implementing the conventional static C_G and proposed dynamic C_G models, respectively (see Fig. 19). During turn-ON transient [see Fig. 19(a)], the calculated i_D waveform with proposed dynamic C_G model shows better agreement with the measured waveform. Fig. 19(b) shows the measured and calculated switching transient waveforms during turn-OFF transient by implementing the static C_G and dynamic C_G models, respectively. Compared with the conventional static C_G model, the proposed dynamic C_G model with larger C_{iss} can yield lower dv_{DS}/dt and di_D/dt, leading to better agreement with the measured switching transients. In summary, compared with the conventional static C_G model, in addition to the enhanced accuracy in the DPTs, the proposed dynamic C_G model can yield more accurate switching transient calculation in dc–dc converter as well.

V. Conclusion

In this article, the dynamic C_G model by considering its dependence on both V_{DS} and V_{GS} ($C_G(V_{DS}, V_{GS})$) during switching transient has been established, according to the gate charge storage of p-GaN gate HEMT. The proposed dynamic $C_G(V_{DS}, V_{GS})$ model has been validated by C_G measurement results with varying V_{DS} and V_{GS}. By analyzing the impact of 2DEG accumulation on C_{GD} during switching, the dynamic $C_G(V_{DS}, V_{GS})$ model yields more accurate C_{GD} that agrees well with that in the measured switching transient. Compared with the conventional static C_G characteristics that neglect the dependence of C_G on varying V_{GS} during switching, the switching analytical model implementing the dynamic $C_G(V_{DS}, V_{GS})$ characteristics can deliver better accuracy in the switching transient calculation. The modeling approach and the dynamic $C_G(V_{DS}, V_{GS})$ model specifically for high-speed GaN HEMT are valuable for accurate switching transient analysis and high-frequency power converter design.

REFERENCES

[1] K. J. Chen et al., "GaN-on-Si power technology: Devices and applications," *IEEE Trans. Electron Devices*, vol. 64, no. 3, pp. 779–795, Mar. 2017.

[2] X. Wu and H. Shi, "High efficiency high density 1 MHz 380–12V DCX with low FoM devices," *IEEE Trans. Ind. Electron.*, vol. 67, no. 2, pp. 1648–1656, Feb. 2020.

[3] A. Lemmon, M. Mazzola, J. Gafford, and C. Parker, "Instability in half-bridge circuits switched with wide band-gap transistors," *IEEE Trans. Power Electron.*, vol. 29, no. 5, pp. 2380–2392, May 2014.

[4] R. Xie, H. Wang, G. Tang, X. Yang, and K. J. Chen, "An analytical model for false turn-on evaluation of high-voltage enhancement-mode GaN transistor in bridge-leg configuration," *IEEE Trans. Power Electron.*, vol. 32, no. 8, pp. 6416–6433, Aug. 2017.

[5] K. Wang, X. Yang, L. Wang, and P. Jain, "Instability analysis and oscillation suppression of enhancement-mode GaN devices in half-bridge circuits," *IEEE Trans. Power Electron.*, vol. 33, no. 2, pp. 1585–1596, Feb. 2018.

[6] J. Chen, X. Du, Q. Luo, X. Zhang, P. Sun, and L. Zhou, "A review of switching oscillations of wide bandgap semiconductor devices," *IEEE Trans. Power Electron.*, vol. 35, no. 12, pp. 13182–13199, Dec. 2020.

[7] K. Wang, X. Yang, H. Li, H. Ma, X. Zeng, and W. Chen, "An analytical switching process model of low-voltage eGaN HEMTs for loss calculation," *IEEE Trans. Power Electron.*, vol. 31, no. 1, pp. 635–647, Jan. 2016.

[8] J. Chen, Q. Luo, J. Huang, Q. He, and X. Du, "A complete switching analytical model of low-voltage eGaN HEMTs and its application in loss analysis," *IEEE Trans. Ind. Electron.*, vol. 67, no. 2, pp. 1615–1625, Feb. 2020.

[9] M. Okamoto, G. Toyoda, E. Hiraki, T. Tanaka, T. Hashizume, and T. Kachi, "Loss evaluation of an AC-AC direct converter with a new GaN HEMT SPICE model," in *Proc. IEEE Energy Convers. Congr. Expo.*, 2011, pp. 1795–1800.

[10] J. P. Kozak et al., "An analytical model for predicting turn-on overshoot in normally-off GaN HEMTs," *IEEE J. Emerg. Sel. Top. Power Electron.*, vol. 8, no. 1, pp. 99–110, Mar. 2020.

[11] Z. Dong, X. Wu, H. Xu, N. Ren, and K. Sheng, "Accurate analytical switching-on loss model of SiC MOSFET considering dynamic transfer characteristic and Q_{gd}," *IEEE Trans. Power Electron.*, vol. 35, no. 11, pp. 12264–12273, Nov. 2020.

[12] R. Xie et al., "Switching transient analysis for normally-off GaN transistor with p-GaN gate in a phase-leg circuit," *IEEE Trans. Power Electron.*, vol. 34, no. 4, pp. 3711–3728, Apr. 2019.

[13] C. Sun, Z. Niu, and S. Yang, "Dynamic gate capacitance model for switching transient analysis in p-GaN gate HEMTs," in *Proc. 35th Int. Symp. Power Semicond. Devices IC's*, 2023, pp. 135–138.

[14] Z. Liu, X. Huang, F. C. Lee, and Q. Li, "Package parasitic inductance extraction and simulation model development for the high-voltage cascode GaN HEMT," *IEEE Trans. Power Electron.*, vol. 29, no. 4, pp. 1977–1985, Apr. 2014.

[15] D. Delagebeaudeuf and N. T. Linh, "Metal-(n)AlGaAs-GaAs two-dimensional electron gas FET," *IEEE Trans. Electron Devices*, vol. ED-29, no. 6, pp. 955–960, Jun. 1982.

[16] J. E. Meyer, "MOS models and circuit simulation," *RCA Rev.*, vol. 32, no. 1, pp. 42–63, Mar. 1971.

[17] S. Karmalkar and U. K. Mishra, "Enhancement of breakdown voltage in AlGaN/GaN high electron mobility transistors using a field plate," *IEEE Trans. Electron Devices*, vol. 48, no. 8, pp. 1515–1521, Aug. 2001.

[18] Y. Wu et al., "An actively-passivated p-GaN gate HEMT with screening effect against surface traps," *IEEE Electron Device Lett.*, vol. 44, no. 1, pp. 25–28, Jan. 2023.

[19] J. Yu et al., "650-V E-mode p-GaN gate HEMT with schottky source extension towards enhanced short-circuit reliability," *IEEE Electron Device Lett.*, vol. 44, no. 10, pp. 1700–1703, Oct. 2023.

[20] GS66508B Datasheet, GaN Systems, Accessed: Apr. 2020. [Online]. Available: https://gansystems.com/wp-content/uploads/2020/04/GS66508B-DS-Rev-200402.pdf

[21] M. Guacci, D. Bortis, and J. W. Kolar, "On-state voltage measurement of fast switching power semiconductors," *CPSS Trans. Power Electron. Appl.*, vol. 3, no. 2, pp. 163–176, Jun. 2018.

Jiahong Du (Graduate Student Member, IEEE) received the B.Eng. degree in electronic science and technology from Hefei University of Technology, Hefei, China, in 2021. He is currently working toward the Ph.D. degree in integrated circuit engineering with the University of Science and Technology of China, Hefei, China.

His current research interests include the characterization and application-relevant study of GaN-based power devices.

Caien Sun (Student Member, IEEE) received the B.S. degree from the Harbin Institude of Technology, Harbin, China, in 2021, and the M.S. degree from Zhejiang University, Hangzhou, China, in 2024, all in electrical engineering.

His research interests include characterization and modeling of GaN-based power devices.

Qiuyi Tang received the B.Eng. degree in electronic science and technology in 2023 from the University of Sience and Technology of China, Hefei, China, where he is currently working toward the M.S. degree in electronic science and technology with the School of Microelectronics.

His current research interests include characterization and modeling of GaN-based power devices.

Bomin Jiang received the B.S. degree in applied physics from Shanghai University, Shanghai, China, in 2022. He is currently working toward the M.S. degree in integrated circuit engineering with the University of Science and Technology of China, Hefei, China.

His current research interests include the characterization and modeling of GaN-based power devices.

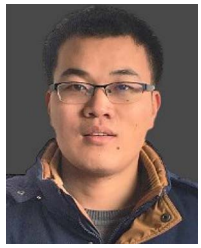

Zezheng Dong (Member, IEEE) received the B.S. and Ph.D. degrees in electrical engineering from the College of Electrical Engineering, Zhejiang University, Hangzhou, China, in 2014 and 2021, respectively.

From 2022 to 2024, he was a Postdoctoral Researcher with Hangzhou Global Scientific and Technological Innovation Center and the College of Electrical Engineering, Zhejiang University. He is currently a full-time Principal Investigator with the Hangzhou Global Scientific and Technological Innovation Center, Zhejiang University. His research interests include packaging and characterizing of wide bandgap power devices.

Xinke Wu (Senior Member, IEEE) received the B.S. and M.S. degrees from the Harbin Institute of Technology, Harbin, China, in 2000 and 2002, respectively, and the Ph.D. degree from Zhejiang University, Hangzhou, China, in 2006, all in electrical engineering.

From 2007 to 2009, he was a Postdoctoral Fellow with the National Engineering Research Center for Applied Power Electronics, Zhejiang University. Since 2009, he has been an Assistant Research Fellow, and then, from 2011 to 2015, as an Associate Professor with the Institute of Power Electronics, Zhejiang University, where he is currently a Professor. From 2011 to 2012, he was a Visiting Scholar with the Center of Power Electronics System, Virginia Tech. His research interests include high-frequency and high-efficiency power conversion, and power electronics system integration.

Dr. Wu was the recipient of the Distinguished Young Scholar Award from Zhejiang University in 2012, the Young Scholar Award from NSF of China in 2015, and two Best Paper Awards from IEEE TRANSACTIONS ON POWER ELECTRONICS. He is the Co-Editor-in-Chief of *Power Electronics Letter*, an Associate Editor for IEEE TRANSACTIONS ON POWER ELECTRONICS and *CPSS Transactions on Power Electronics and Applications*.

Shu Yang (Senior Member, IEEE) received the B.S. degree in microelectronics from Fudan University, Shanghai, China, in 2010, and the Ph.D. degree in electronic and computer engineering from the Hong Kong University of Science and Technology (HKUST), Hong Kong, China, in 2014.

She was a Visiting Assistant Professor with HKUST, a Post-Doctoral Research Associate with the University of Cambridge, Cambridge, U.K, and a Professor with Zhejiang University, Hangzhou, China. She is currently a Professor with the School of Microelectronics, University of Science and Technology of China, Hefei, China. Her research interests include the fabrication, characterization, and application-relevant study of GaN-based power devices.

Dr. Yang was the recipient of IEEE ISPSD Charitat Young Researcher Award and Delta Young Scholar Award. She was a Guest Associate Editor for IEEE JOURNAL OF EMERGING AND SELECTED TOPICS IN POWER ELECTRONICS.